



1 **Sources and trends of Black Carbon Aerosol in a Megacity of Nanjing,**  
2 **East China After the China Clean Action Plan and Three-Year Action**  
3 **Plan**

4 *Abudurexiati·Abulimiti<sup>a,b</sup>, Yanlin Zhang<sup>a,b\*</sup>, Mingyuan Yu<sup>a,b</sup>, Yihang Hong<sup>a,b</sup>, Yu-Chi Lin<sup>a,b</sup>,*  
5 *Chaman Gul<sup>c</sup>, Fang Cao<sup>a,b</sup>*

6 *<sup>a</sup> School of Ecology and Applied Meteorology, Nanjing University of Information Science and*  
7 *Technology, Nanjing, 210044, China*

8 *<sup>b</sup> Atmospheric Environmental Center, Joint Laboratory for International Cooperation on*  
9 *Climate and Environmental Change, Ministry of Education, Nanjing University of Information*  
10 *Science and Technology, Nanjing, 210044, China*

11 *<sup>c</sup> Reading Academy, Nanjing University of Information Science and Technology, Nanjing,*  
12 *Jiangsu, 210044, China*

13 *Correspondence to:*

14 Yanlin Zhang\* ([zhangyanlin@nuist.edu.cn](mailto:zhangyanlin@nuist.edu.cn), [dryanlinzhang@outlook.com](mailto:dryanlinzhang@outlook.com))

15 **Abstract** Black carbon (BC) is an essential component of particulate matter  
16 (PM) with a significant impact on climate change. Few studies have  
17 investigated the long-term changes in BC and the sources, particularly  
18 considering primary emissions of BC, which is crucial for developing  
19 effective mitigation strategies. Here, based on three-year observations (2019-  
20 2021), random forest (RF) algorithms were employed to reconstruct BC  
21 concentrations in Nanjing from 2014 to 2021. Source apportionment was  
22 conducted on the reconstructed data to investigate long-term trends of BC and  
23 its sources. The results showed that the three-year average BC concentration  
24 was  $2.5 \pm 1.6 \mu\text{g m}^{-3}$ , peaking in winter, with approximately 80% attributed to  
25 liquid fuel combustion. Notably, the reconstructed time series revealed a  
26 significant decrease ( $p < 0.05$ ) in BC levels over the eight-year period,  
27 primarily due to reduced emissions from liquid fuels. The comparison  
28 between two control polices periods (P1:2014-2017 and P2:2018-2021)  
29 indicate that BC concentrations decline more steeply during S2 since  
30 significant ( $p < 0.05$ ) reduction in biomass burning. The seasonal analysis  
31 showed significant reductions ( $p < 0.05$ ) in BC, BC<sub>liquid</sub> (black carbon from  
32 liquid fuel combustion) and BC<sub>solid</sub> (black carbon from solid fuel combustion)  
33 during winter, with BC<sub>liquid</sub> accounting for 77% of the reduction. Overall,  
34 emission reduction was the dominant factor in reducing BC levels,  
35 contributing between 62% and 86%, as revealed by Kolmogorov-Zurbenko



36 (KZ) filter. However, during P2, meteorological conditions played a more  
37 significant role, especially in reducing BC and BC<sub>liquid</sub>, with an increase in  
38 their impact on BC<sub>solid</sub> compared to P1. Our results demonstrated that target  
39 control measures for liquid fuel combustion are necessary, as liquid fuel  
40 combustion is a major driver of decreasing BC, especially in summer, while  
41 the influence of meteorological factors on BC variations cannot be overlooked.

42 **Keywords:** black carbon; sources; random forest; emission reduction

### 43 **1. Introduction**

44 Black carbon (BC), also known as element carbon (EC), is a  
45 carbonaceous component of particulate matter (PM) produced through  
46 incomplete combustion processes, including domestic cooking, heating and  
47 coke-making (Bond et al., 2013; Liu et al., 2020). BC particles significantly  
48 influence the Earth's energy balance and are major contributors to global  
49 warming due to their strong absorption of solar radiation across visible to  
50 infrared wavelengths (Ramanathan and Carmichael, 2008; Ipcc, 2023).  
51 Additionally, the presence of BC particles in the atmosphere reduces  
52 atmospheric visibility and deteriorates air quality especially in urban areas  
53 due to their significant absorption properties (Ding et al., 2016). Exposure to  
54 BC aerosols has also been linked to increased health risks, such as heart  
55 attacks and cardiovascular diseases (Sarigiannis et al., 2015; Li et al., 2019).  
56 Owing to its short atmospheric lifetime of only 3 to 14 days, much shorter  
57 than that of greenhouse gases which can persist for decades, reducing BC  
58 emissions can promptly mitigate global warming and benefit human health.

59 Accurate quantification of BC from different sources is essential to  
60 propose efficient mitigation strategies. Various methods in the past have been  
61 applied to BC source apportionment, including emission inventories (Zhu et  
62 al., 2020), radiocarbon isotope analysis (Zhang et al., 2014; Yu et al., 2023),  
63 and receptor models (Zong et al., 2016). However, uncertainties arise due to  
64 the lack of reliable emission factors, and receptor models require additional  
65 aerosol composition data. The radiocarbon source apportionment method is  
66 limited by its low temporal resolution, which hinders their ability to capture  
67 the dynamic changes in BC sources. In contrast, the Aethalometer model,  
68 with its high temporal resolution and rapid analysis, has been widely adopted  
69 for quantifying BC derived from liquid fuel (BC<sub>liquid</sub>) and solid fuel (BC<sub>solid</sub>)  
70 combustion (Lin et al., 2021; Sandradewi et al., 2008; Helin et al., 2018).



71 To address the severe air pollution issue, the Chinese government  
72 implemented the “China Clean Action Plan” during 2013-2017 and the  
73 “Three-Year Action Plan” during 2018-2020. Several studies in recent years  
74 have focused on long-term BC mass concentrations in major cities or regions  
75 of China to evaluate the impact of emission reduction measures implemented  
76 by the Chinese government (Sun et al., 2022a; He et al., 2023). However,  
77 while most of these studies document changes in BC concentrations, few have  
78 explored the specific contributions of different BC sources. Such an  
79 understanding is essential for identifying the drivers behind observed changes  
80 and for developing targeted mitigation strategies. Moreover, comprehensive  
81 datasets of BC are crucial for a better understanding of BC mass concentration  
82 variations and their implications for air quality policy. However, newly  
83 established monitoring stations often lack sufficient long-term observations,  
84 making it difficult to evaluate historical variations in BC concentrations. This  
85 limitation hinders efforts to understand BC dynamics in regions with limited  
86 prior monitoring, ultimately complicating the formulation of effective  
87 emission reduction policies. Chemical transport models (CTMs), which  
88 integrate meteorological conditions and emission inventories, are effective in  
89 simulating near-surface BC concentrations over short term periods (Cheng et  
90 al., 2019; Zhou et al., 2023). Nonetheless, their computational intensity and  
91 time-consuming often limit their application to long-term simulation. In  
92 contrast, the prediction of PM or other air pollutants can be efficiently  
93 achieved through statistical models that establish relationships between  
94 measured values and various variables, including co-emitted pollutants, air  
95 humidity and air temperature. Recently, the historical values of nitrate  $\delta^{15}\text{N}$   
96 and  $\text{PM}_{2.5}$  have been accurately reproduced based on the statistical  
97 relationships established between measured variables and other influencing  
98 factors (Fan et al., 2023; Zhao et al., 2020; Wu et al., 2024). This method  
99 provides a relatively straightforward approach for simulating historical air  
100 pollutants and is accurate enough for examining their long-term variations.

101 The long-term variation of atmospheric aerosol composition can be  
102 attributed to both meteorology conditions and emissions. CTMs are one of the  
103 often used tools to quantify the impact of meteorology and emission on  
104 aerosols, as they consider the physical and chemical process that air pollutants  
105 undergo during their time in the atmosphere (Li et al., 2023; Zhang et al., 2019;



106 Du et al., 2022). However, the accuracy of CTMs is often constrained by their  
107 initial conditions and uncertainty in emission inventory as well as models'  
108 underlying assumptions. Another commonly used method for separating the  
109 influences meteorology and emissions on target atmospheric pollutants is the  
110 Kolmogorov-Zurbenko (KZ) filter. For example, Sun et al. (2022b) found that  
111 meteorological contribution to the PM<sub>2.5</sub> trend presented a distinct spatial  
112 pattern over the Twain-Hu Basin, with northern positive rates up to 61% and  
113 southern negative rates down to -25%. Chen et al. (2019) reported that  
114 anthropogenic emissions contributed to 80% of reduction in PM<sub>2.5</sub> in Beijing  
115 from 2013 to 2017. Compared to CTMs, the KZ filter is easier to operate and  
116 is suitable for any long-term datasets of air pollutants, making it a practical  
117 tool for analyzing trends in atmospheric pollutants.

118 In the present study, a three-year BC mass concentration measurement  
119 was conducted to clarify BC characteristics and quantify contributions from  
120 different sources. The measured BC at two wavelengths (370nm and 880 nm)  
121 then incorporated into random forest model to establish the nonlinear  
122 relationships with predictor variables, such as air pollutants and  
123 meteorological factors. Historical BC concentrations at the two wavelengths  
124 were reconstructed from 2014-2021 using the trained models to investigate  
125 the long-term temporal variation of BC and sources, with a focus on the two  
126 distinct emission reduction periods: the “China Clean Action Plan” and the  
127 “Three-Year Action Plan”. Finally, the impacts of meteorology and emissions  
128 on the long-term trend of BC were quantified to provide deeper insights into  
129 the factors driving its historical changes.

## 130 **2. Data and Methods**

### 131 **2.1 Sampling site and Data**

132 Nanjing is located eastern part of China, is vital industrial and economic  
133 center. The sampling instrument used for monitoring BC mass concentration  
134 was positioned on the rooftop of a seven-story building at the campus of  
135 Nanjing Information Science and Technology (NUSIT, 32.21°N, 118.72°E,  
136 Figure S1 in Supporting Information), Nanjing, China. The sampling site  
137 represents a typical urban atmospheric environment, encircled by local roads  
138 with an expressway approximately 1 km away. Moreover, a steel  
139 manufacturing plant and a petroleum chemical factory were about 5 km away  
140 from the sampling site. Traffic and industrial emissions are the primary



141 sources of air pollution at the sampling site. Nanjing experiences four  
142 dominant seasons each year: winter (December-February), spring (March-  
143 May), summer (June-August), and autumn (September-November).

144 A dual-spot Aethalometer (AE33, Magee Scientific) was used to  
145 measure BC mass concentration from January 2019 to December 2021. The  
146 flow rate of AE33 was set to 5 L min<sup>-1</sup> and the inlet cut-off size was 2.5 μm  
147 throughout the entire period. In brief, aerosol particles were collected on a  
148 filter tape automatically, and light attenuations (ATN) were measured at seven  
149 distinct spectral regions (370, 470, 520, 590, 660, 880, 950 nm) with a time  
150 resolution of 1 min. The ATNs were then converted to BC mass  
151 concentrations with seven different mass absorption cross sections (18.47,  
152 14.54, 13.14, 11.58, 10.35, 7.77, 7.19 m<sup>2</sup> g<sup>-1</sup>). In this study the BC  
153 concentration calculated by 880 nm spectral region was used, as BC is the  
154 predominant absorber at this wavelength (Drinovec et al., 2015). The BC data  
155 was missing since instrument maintenance from 13<sup>th</sup> July to 31<sup>st</sup>, 2020, and  
156 from July 23<sup>rd</sup> to September 26<sup>th</sup>, 2021. Hourly averaged concentrations of  
157 PM<sub>2.5</sub>, CO, SO<sub>2</sub> and NO<sub>2</sub> were obtained from the China National Air Quality  
158 Monitoring Station, located approximately 10 km from the sampling site.  
159 Hourly resolution meteorological data, including temperature (T), relative  
160 humidity (RH), wind speed (WS), wind direction (WD) and boundary layer  
161 height (BLH), were sourced from the ERA5 reanalysis datasets provided by  
162 the European Centre for Medium-Range Weather Forecasts (ECMWF).

## 163 **2.2 Aethalometer measurements and source apportionment**

164 The absorption Ångström exponent (AAE) describes the spectral  
165 dependence of BC and is determined through a power-law fit between light  
166 absorption ( $b_{abs}(\lambda)$ ) and seven wavelengths, the equation can be written as:

$$b_{abs}(\lambda) = \beta \cdot \lambda^{-AAE} \quad (1)$$

167 where  $\beta$  is a constant dependent on aerosol mass concentration and size  
168 distribution. Subsequently, the Aethalometer model is utilized to quantify the  
169 contribution of liquid and solid fuels to BC. The model assumes that ambient  
170 BC primarily originates from liquid fuel and solid fuel combustion, with BC  
171 from two distinct combustion sources having differing light absorption  
172 spectra. Hence, the total light absorption at 880 nm is attributed to liquid fuel-  
173 generated BC (BC<sub>liquid</sub>) and solid fuel-derived BC (BC<sub>solid</sub>). The relationships



174 between  $b_{abs}(\lambda)$ ,  $\lambda$  and AAE can thus be expressed as follows:

$$\frac{b_{abs}(\lambda_1)_{liquid}}{b_{abs}(\lambda_2)_{liquid}} = \left(\frac{\lambda_1}{\lambda_2}\right)^{-AAE_{liquid}} \quad (2)$$

175

$$\frac{b_{abs}(\lambda_1)_{solid}}{b_{abs}(\lambda_2)_{solid}} = \left(\frac{\lambda_1}{\lambda_2}\right)^{-AAE_{solid}} \quad (3)$$

176

$$b_{abs}(\lambda) = b_{abs}(\lambda)_{liquid} + b_{abs}(\lambda)_{solid} \quad (4)$$

177 where  $AAE_{liquid}$  and  $AAE_{solid}$  are the AAE values of BC from liquid and solid  
178 fuel combustion,  $\lambda_1$  and  $\lambda_2$  are of different wavelengths. The selection of  
179 wavelengths (370-880 nm and 470-950 nm) can impact source apportionment  
180 results. Here, the 470 nm and 950 nm were chosen as they were recommended  
181 in the Aethalometer model (Drinovec et al., 2015). Moreover, source  
182 apportionment result of the Aethalometer model highly depend on selection  
183 of AAE pairs, with the value of AAE being determined by the type of biomass,  
184 combustion processes and long-ranged transport condition (Gul et al., 2021).  
185 The effect of different AAE values on the results discussed in section 3.3.2  
186 (source diagnostic tracer). Combining the equations (2) ~ (4), we can obtain  
187 the contribution of solid fuel combustion (BB%) to total BC:

$$BB(\%) = \frac{b_{abs}(\lambda_2)_{solid}}{b_{abs}(\lambda_2)} \times 100\% \quad (5)$$

188 Then, the  $BC_{solid}$  can be obtained as follows:

$$BC_{solid} = BC(880nm) \times BB(\%) \quad (6)$$

189 Finally, the  $BC_{liquid}$  can be calculated as:

$$BC_{liquid} = BC(880nm) - BC_{solid} \quad (7)$$

### 190 **2.3 Building random forest model and tuning hyper parameters**

191 The random forest (RF) machine learning algorithm is utilized to  
192 reproduce historical time series data of BC. RF, a model comprising hundreds  
193 of decision trees, splits data based on the informative features to avoid  
194 overfitting. However, decision trees can easily overfit, resulting in inaccurate  
195 model predictions. RF selects random samples of observation data for each  
196 decision tree, a common problem in decision trees, by using random data



197 samples for each tree. The RF algorithm has been effectively applied in  
198 atmospheric chemistry regions for predicting PM<sub>10</sub> and organic carbon (OC)  
199 in different regions (Grange et al., 2018; Qin et al., 2022), demonstrating its  
200 strong predictive capabilities.

201 In this work, the BC concentrations from 2019-2021 (target variables)  
202 along with pollutants gases (SO<sub>2</sub>, CO, NO<sub>2</sub>) and meteorology factors such as  
203 T, RH, WS, WD and BLH (independent variables) were inputted into RF  
204 models. To train the RF model and assess the predicting ability of three RF  
205 models, the whole dataset was randomly divided into training and testing sets  
206 in a ratio of 8:2. Given that observational data followed a log-normal  
207 distribution, most of the data are concentrated within a specific interval,  
208 resulting a poor model performance on extreme values. To ensure a good  
209 model performance, some data augmentation methods were used to achieve  
210 data balance by interpolating or duplicating the less frequent data, ensuring  
211 that the overall data essentially conforms to a uniform distribution (Hong et  
212 al., 2023; Huang et al., 2023). To obtain optimal hyperparameter values, 10-  
213 fold cross-validation was utilized on the training sets, dividing the datasets  
214 into 10 subsamples, where 9 subsamples were used for training data and 1  
215 subsample for testing. Optimized parameters for the models were chosen  
216 based on the best mean squared error (MAE), root mean squared error (RMSE)  
217 and R square (R<sup>2</sup>) values obtained from the 10-fold cross-validation. Finally,  
218 the test sets were then put into models and evaluated model predicting abilities.  
219 The optimized parameters selected for the models are presented in Table 1.  
220 The BC monitored by Aethalometer at 370 nm wavelength was also predicted  
221 by RF models with same independent variables to explore the changes in BC  
222 sources in Nanjing from 2014 to 2021.

223 Table 1 Parameters used in random forest models

Parameters	Range	Optimal value	
		BC_880nm	BC_370nm
n_estimators	[100-350]	95	100
max_depth	[10-30]	25	23
max_feature	[auto, sqrt, log2]	sqrt	sqrt
criterion	[friedman_mse, poisson, squared_error, absolute_error]	absolute_error	absolute_error

## 224 2.4 Kolmogorov-Zurbenko filter



225 The KZ filter, a method for decomposing time series data into distinct  
226 components, is widely utilized in air pollutants studies to differentiate the  
227 influence of meteorology and emissions strength on the long-term trend of air  
228 pollutants (Wise and Comrie, 2005; Yin et al., 2019; Chen et al., 2019). Since  
229 the original concentration of BC follows a log-normal distribution, the data  
230 ( $\chi$ ) were transformed into natural logarithmic form ( $X = \ln(\chi)$ ) before  
231 applying the KZ filter, allowing the data follow normally distribution (Zheng  
232 et al., 2023). The KZ filter assumes that the original time series of a certain  
233 air pollutant comprises short-term, seasonal, and long-term components. Thus,  
234 the original time series of BC [ $X(t)$ ] can be expressed as:

$$X(t) = E(t) + S(t) + W(t) \quad (8)$$

235 Here,  $E(t)$  represents the long-term component, mainly affected by climate,  
236 long-range transport of air pollutants and emission intensity changes due to  
237 shifts in energy structure.  $S(t)$  is the seasonal component, attributed to  
238 variations in meteorology conditions and emission intensity across different  
239 seasons.  $W(t)$  is the short-term component driven by weather patterns and  
240 fluctuations in local-scale emissions.

241 The KZ filter is a low-pass filter characterized by a window length ( $m$ )  
242 and iterations ( $p$ ). Different ‘ $m$ ’ and ‘ $p$ ’ values can be used to separate each  
243 component of an air pollutant.  $KZ_{(15,5)}$  can eliminate cycles that are less than  
244 33 days and obtain the baseline component of the original data. The  $W(t)$  can  
245 be easily obtained by subtracting  $X_{BL}(t)$  from  $X(t)$ . Therefore, the long-term,  
246 short-term and seasonal components can be extracted as follows:

$$X_{BL}(t) = KZ_{(15,5)}[X(t)] = X(t) - W(t) \quad (9)$$

248 The  $X_{BL}$  is assumed to consist of its repeated climatological seasonal cycle  
249 ( $X_{BL}^{clm}$ ) and residuals ( $\varepsilon$ ).

$$X_{BL} = X_{BL}^{clm}(t) + \varepsilon \quad (10)$$

251 The  $X_{BL}^{clm}$  contains most of the seasonality in  $X_{BL}$ , while  $\varepsilon$  consist of  $E(t)$  along  
252 with minor seasonal variability unconsidered in  $X_{BL}^{clm}$ . Applying a KZ filter  
253 with a window length of 365 and an iteration of 3 ( $KZ_{(365,3)}$ ) to  $\varepsilon$ , the  $E(t)$  and  
254  $S(t)$  can be obtained:

$$E(t) = KZ_{(365,3)}[\varepsilon(t)] = X_{BL}(t) - S(t) \quad (11)$$





256 Due to emissions and meteorological condition changes can be both influence  
257 on long-term trend of BC, the long-term component can be assumed to consist  
258 of emission-related ( $E_{LT}^{emi}$ ) and meteorology-related ( $E_{LT}^{met}$ ) components. Thus,  
259 the  $X_{BL}$  can be expressed as follows:

$$260 \quad X_{BL}(t) = S(t) + E_{LT}^{emi} + E_{LT}^{met} \quad (12)$$

261 To derive the  $E_{LT}^{emi}$  in Eq.(9), the multiple linear regression model was  
262 conducted baseline component of BC along with baseline components of six  
263 meteorological factors such as T, RH, WS, WD, BLH, surface pressure (SP).  
264 Then, the formulas can be written as follows:

$$X_{BL}(t) = a_0 + \sum_i a_i MET_{BL} + \varepsilon' \quad (13)$$

265 Where  $a_0$  is the intercepts of multiple linear regression model outcomes.  
266  $MET_{BL}$  denote the baseline components of meteorology factors which are  
267 obtained by KZ<sub>(15,5)</sub>.  $\varepsilon'$  is the sum of emission-related long-term variability  
268 and some minor seasonal variability unexplained by the multiple linear  
269 regression model. Therefore, the  $E_{LT}^{emi}$  can be extracted by applying KZ<sub>(365,3)</sub>  
270 to  $\varepsilon'$ . Then, the  $E_{LT}^{met}$  can be obtained by subtracting  $E_{LT}^{emi}$  from long-term  
271 component ( $E(t)$ ) (Seo et al., 2018).

$$272 \quad E_{LT}^{emi}(t) = KZ_{(365,3)}[\varepsilon'(t)] = E(t) - E_{LT}^{met}(t) \quad (14)$$

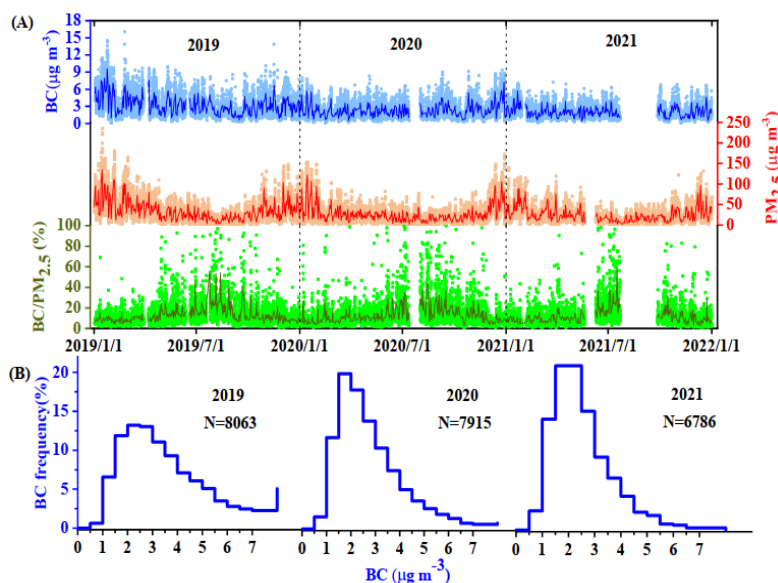
### 273 **3 Results and Discussion**

#### 274 **3.1 General characteristic of BC in Nanjing**

275 Figure 1(a) shows the hourly (dots) and daily (line) mean variation of  
276 BC,  $PM_{2.5}$  mass concentrations, and the proportion of BC to  $PM_{2.5}$  in Nanjing.  
277 A 400-fold variation was found in hourly BC concentration, which ranged  
278 from 0.04 to 16.05  $\mu g m^{-3}$ . Daily BC levels fluctuated much less than hourly  
279 concentration, from the lowest value of 0.40  $\mu g m^{-3}$  (15<sup>th</sup> May 2021) to the  
280 highest value of 9.58  $\mu g m^{-3}$  (24<sup>th</sup> January 2019). The average BC level during  
281 the whole sampling period was  $2.52 \pm 1.62 \mu g m^{-3}$ . Figure 1(b) illustrates the  
282 frequency distributions of hourly BC concentrations during different  
283 sampling periods. Over three years, BC distributions shifted toward lower  
284 values. In 2019, the most frequent BC concentrations were observed in 2 to 3  
285  $\mu g m^{-3}$  range, accounting for 26.2% of samples. In 2020 and 2021, the most  
286 BC levels were found in the 1 to 2  $\mu g m^{-3}$  range, with frequencies of 38.0%



287 and 41.9%, respectively. BC levels exceeding  $7 \mu\text{g m}^{-3}$  accounted for 5.1%,  
288 0.8% and 0.01% in three years.  $\text{PM}_{2.5}$  showed a similar variation to BC, with  
289 a significant correlation ( $r = 0.74$ ,  $p < 0.05$ ) observed between daily  $\text{PM}_{2.5}$  and  
290 BC concentrations during sampling period. The hourly ratio of BC to  $\text{PM}_{2.5}$   
291 varied from 0.1 to 99%, with an annual mean of 12%. Compared to a previous  
292 study conducted in Yangtze River Delta, the BC/ $\text{PM}_{2.5}$  ratio in Nanjing was  
293 much higher than Shanghai (5.6%) (Wei et al., 2020), implying a greater  
294 importance of primary emissions in Nanjing.



295  
296 Figure 1 (A) Hourly (dots) and daily (line) concentration of BC,  $\text{PM}_{2.5}$  and BC/ $\text{PM}_{2.5}$  and (b) frequency  
297 of BC for each year during 2019, 2020 and 2021. N represents number of hourly BC concentration for  
298 one year

299 Table 2 listed long-time (equal or more than one year) BC mass  
300 concentrations monitored by optical method in Nanjing and other sampling  
301 sites all over the world from previous studies. Nanjing's three-year average  
302 BC level was the lowest among previous studies performed in Nanjing,  
303 indicating that primary emissions in Nanjing are decreasing year by year.  
304 While BC levels in other southern Chinese cities like Shanghai and Wuhan  
305 were at least 12.0% lower than those in Nanjing, they were at least 13.9%  
306 higher in northern Chinese cities like Beijing and Baoji. Additionally, BC  
307 concentrations in Nanjing were five times higher than in the baseline station



308 Mt. Waliguan.

309 Table 2 Comparison of BC mass concentration in Nanjing with other sites

Location	Site type	Instrument	Study period (yyyy.mm)	BC ( $\mu\text{g m}^{-3}$ )	Reference
Nanjing, China	urban	AE33	2019.01- 2021.12	$2.52 \pm 1.62$	Present study
Nanjing, China	suburban	AE31	2012.01- 2012.12	$4.2 \pm 2.6$	(Zhuang et al., 2014)
Nanjing, China	urban	MAAP <sup>a</sup>	2017.12- 2018.11	$2.8 \pm 2.0$	(Zhang et al., 2020)
Mt. Waliguan, China	baseline	AE31	2008.01- 2017.12	$0.45 \pm 0.37$	(Dai et al., 2021)
Beijing, China	urban	AE31	2016.01- 2016.12	$3.4 \pm 3.0$	(Li et al., 2022)
Baoji, China	urban	AE31	2015.01- 2015.12	$2.9 \pm 1.7$	(Zhou et al., 2018)
Xianghe, China	rural	AE31	2013.04- 2015.03	$5.4 \pm 4.4$	(Ran et al., 2016)
Shanghai, China	urban	AE33	2017.01- 2017.12	$2.2 \pm 1.3$	(Wei et al., 2020)
Wuhan, China	urban	AE33	2013.06- 2018.12	$1.4 \pm 1.2$	(Zheng et al., 2020)
Panchgaon, India	suburban	AE42	2015.04- 2016.03	$7.2 \pm 0.3$	(Dumka et al., 2019)

310 <sup>a</sup>MAAP: Multi-angle absorption photometer

### 311 3.2 Temporal variation of BC mass concentrations in Nanjing

#### 312 3.2.1 Interannual, seasonal, and monthly variations

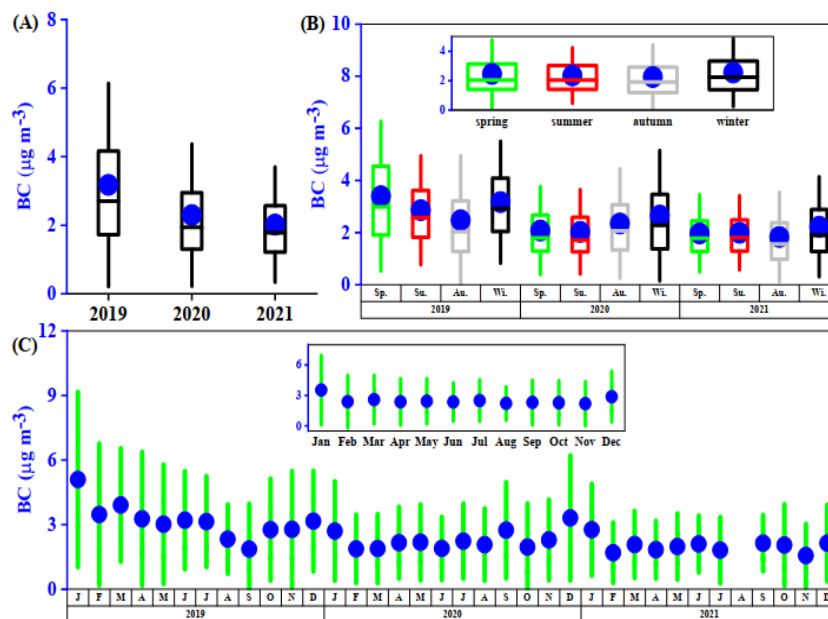
313 The annual, seasonal, and monthly variations in BC mass concentrations  
 314 are illustrated in Figure 2. The annual average BC mass concentration in 2019  
 315 ( $3.2 \pm 2.0 \mu\text{g m}^{-3}$ ) was higher than in 2020 ( $2.3 \pm 1.4 \mu\text{g m}^{-3}$ ) and 2021 ( $2.0 \pm$   
 316  $1.1 \mu\text{g m}^{-3}$ ). A significant reduction of 28.1% in BC mass concentration was  
 317 observed from 2019 to 2020, much higher than the reduction (13.0%)  
 318 observed during 2020-2021. Similarly,  $\text{PM}_{2.5}$  concentrations reduced more  
 319 sharply during 2019-2020 (24.1%) than in 2020-2021 (6.2%). To prevent the



320 spread of COVID-19, a series of lockdown measures were imposed in China  
321 in late January 2020, resulting in a remarkable decrease in concentrations of  
322 air pollutants (Bauwens et al., 2020; Li et al., 2020; Wang et al., 2020).

323 Seasonally, the highest averaged BC level over three years occurred in  
324 winter ( $2.9 \pm 2.0 \mu\text{g m}^{-3}$ ), with no obvious variation identified in spring ( $2.5$   
325  $\pm 1.5 \mu\text{g m}^{-3}$ ), summer ( $2.4 \pm 1.4 \mu\text{g m}^{-3}$ ) or autumn ( $2.3 \pm 1.5 \mu\text{g m}^{-3}$ ),  
326 suggesting a generally locally dominated source of BC emissions. The results  
327 of bivariate polar plots showed the highest BC levels in low wind speed (WS  
328  $< 4 \text{ m s}^{-1}$ ) in all seasons (Figure S2), further indicating that local sources are  
329 the predominant contributors to atmospheric BC in Nanjing. High BC mass  
330 concentrations in winter are mainly caused by enhanced emissions due to cold  
331 weather and deteriorating meteorological dispersion conditions resulting from  
332 low temperatures. A similar seasonal pattern was also found in previous  
333 studies conducted in other Yangtze River Delta cities like Shanghai and Hefei  
334 (Chang et al., 2017; Zhang et al., 2015). Seasonal average concentrations of  
335 BC varied from 1.83 (autumn of 2021) to  $3.40 \mu\text{g m}^{-3}$  (spring of 2019) across  
336 different years. In 2019, BC concentration in spring ( $3.4 \pm 1.9 \mu\text{g m}^{-3}$ ) was  
337 higher than in winter ( $2.6 \pm 1.5 \mu\text{g m}^{-3}$ ), likely due to decreased human  
338 activities during the lockdown period. In contrast to the spring of 2019, higher  
339 levels of BC were found in winter during 2020 and 2021.

340 The monthly mean concentrations of BC showed relatively large  
341 variation, ranging from 1.6 (November of 2021) to  $5.1 \mu\text{g m}^{-3}$  (January of  
342 2019). The highest monthly average BC levels were found in January ( $3.5 \pm$   
343  $2.3 \mu\text{g m}^{-3}$ ), followed by December ( $2.9 \pm 1.7 \mu\text{g m}^{-3}$ ). The monthly variation  
344 pattern of BC is consistent with previous studies in Nanjing, which reported  
345 the highest BC levels in January and December (Zhang et al., 2020; Xiao et  
346 al., 2020). Additionally, the BC concentration in January was 37% higher than  
347 in August ( $2.2 \pm 1.1 \mu\text{g m}^{-3}$ ), attributed to relatively lower emission strength  
348 and larger precipitation in summer in Nanjing.



349  
350 Figure 2 (A) Interannual, (B) seasonal, and (C) monthly variations of BC. The relatively small figures  
351 in (B) and (C) are overall average seasonal and monthly values. The blue dots represent average BC  
352 values. The rectangles in (A) and (B) represent the 25% and 75% quantiles. The vertical lines in (A),  
353 (B), and (C) represent 10% and 90% quantiles.

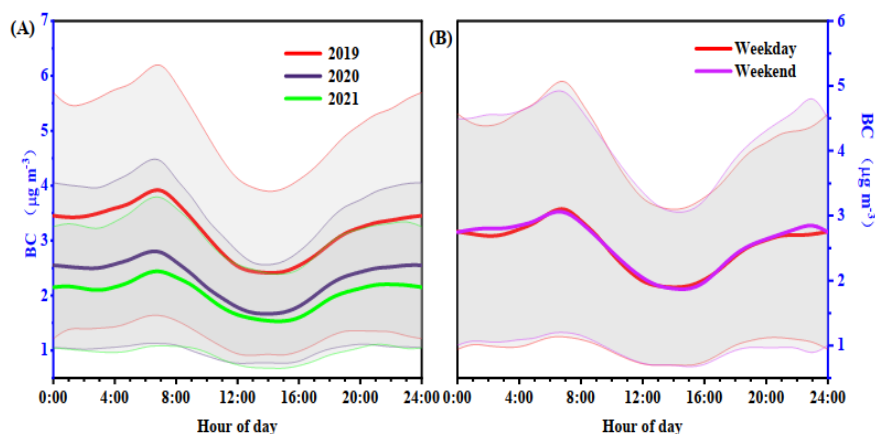
### 354 3.2.2 Diurnal variation of BC

355 The diurnal variations of BC mass concentrations for each year are  
356 plotted in Figure.3(a). The diurnal cycles of BC, like those in previous studies  
357 conducted in Nanjing (Xiao et al., 2020; Zhang et al., 2020; Zhuang et al.,  
358 2014), exhibited bimodal distributions in selected three years. BC mass  
359 concentrations remained relatively flat at midnight and then increased from  
360 3:00 (local time, LT) to 7:00 LT. After reaching the highest values at 7:00 LT,  
361 BC levels decreased, reaching the lowest values at 16:00 LT, then increased  
362 again, and maintaining higher values in the evening. The bimodal diurnal  
363 patterns of BC were attributed to the intensity of emissions and variations in  
364 meteorological conditions (Cao et al., 2009). The morning peak of BC was  
365 mainly caused by vehicle emissions during the traffic rush hour, as indicated  
366 CO and NO<sub>2</sub> also showing similar diurnal cycles to BC (Figure S3). After the  
367 morning peak, the boundary layer height developed and WS increased,  
368 increasing atmospheric dilution capability and lowering the BC levels. After



369 14:00 LT, due to a decrease in boundary layer height and WS, BC was  
370 gathered on the surface layer, resulting in higher BC loading from evening to  
371 midnight. The peak BC concentration in 2019 was 29%, 38% higher than in  
372 2020 and 2021 respectively, indicates air quality in Nanjing is getting better  
373 due to the strict implementation of air pollution control plans. Additionally,  
374 the impact of COVID-19 lockdown measures during selected years have also  
375 contributed to the reduction in BC concentrations.

376 To further explore the impacts of human activities on ambient BC  
377 concentrations, the diurnal variation in BC was separately investigated for  
378 weekdays and weekends. As shown in Figure.3(b), the diurnal patterns of BC  
379 on both weekdays and weekends exhibited bimodal distributions, with similar  
380 peak times at morning vehicle rush hours (7:00 LT), suggesting that local  
381 emission sources of BC in northern Nanjing do not differ significantly  
382 between weekdays and weekends.



383

384 Figure 3 Diurnal variation of BC (A) for each year during 2019-2020 and (B) during weekdays and  
385 weekends. Shaded areas represent the standard deviation at each time of day.

### 386 3.3 Source apportionment of BC

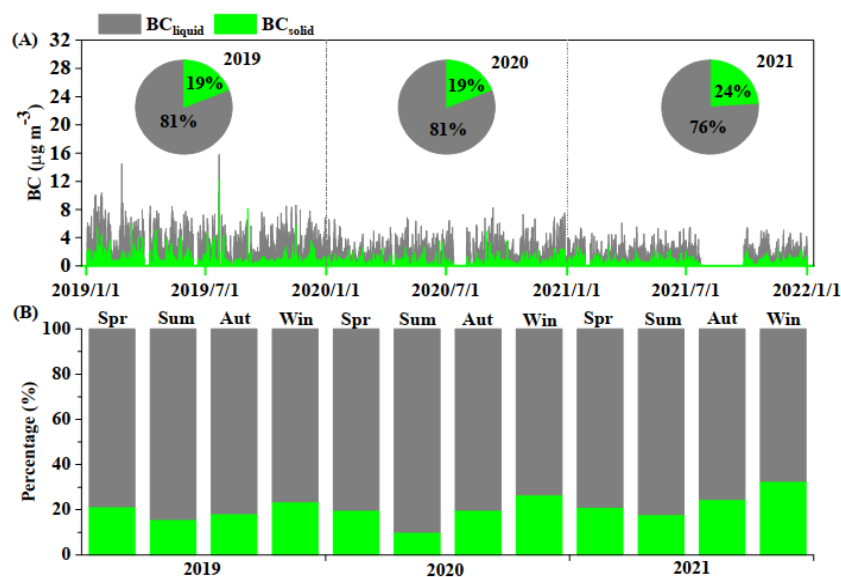
#### 387 3.3.1 Source apportionment of BC by Aethalometer model

388 The AAE values, calculated by power-law fit between light absorbance  
389 and seven wavelengths followed a lognormal distribution in selected three  
390 years, with an hourly variation ranging from 0.71 to 2.59 (Figure S4). The  
391 three-year average AAE value was  $1.25 \pm 0.14$ , with the highest value of  $1.28$   
392  $\pm 0.13$  in 2021, slightly higher by 4.0% and 4.3% in 2019 and 2020,



393 respectively, indicating similar BC emission sources during the sampling  
394 period. Seasonally, the lowest AAE value of  $1.13 \pm 0.14$  was found in summer,  
395 while the highest AAE value of  $1.32 \pm 0.11$  appeared in winter. The monthly  
396 variation of AAE showed a valley in the summer months (particularly in July)  
397 and high values in winter (December), suggesting that Nanjing was  
398 predominantly influenced by traffic-related liquid fuel burning in summer,  
399 and coal-related combustion in winter.

400 To quantify the relative contribution of liquid and solid fuel combustion  
401 to BC concentration, the Aethalometer model, as mentioned in section 2.2,  
402 was applied. The Aethalometer model was initially used for source apportion  
403 BC in Europe, where fossil fuel and biomass burning emissions were two  
404 major sources. However, China's energy structure differs from Europe's, with  
405 coal combustion still playing a significant role. Liu et al. (2018) summarized  
406 AAE values from different coal burning sources in China, finding that AAE  
407 values of coal burning were close to those of biomass combustion. Thus, AAE  
408 values of 1.0 for liquid fuel ( $AAE_{\text{liquid}}$ ) and 2.0 for solid fuel ( $AAE_{\text{solid}}$ ) were  
409 selected for this work. The same AAE pairs were also used for source  
410 apportionment of BC in previous study carried out in Nanjing (Lin et al.,  
411 2021). Figure 4 shows the time series of absolute BC concentrations derived  
412 from liquid and solid fuel combustion, along with a depiction of their relative  
413 contributions to BC in different seasons for each year. The three-year average  
414 concentration of  $BC_{\text{liquid}}$  was  $2.0 \pm 0.5 \mu\text{g m}^{-3}$ , approximately four times that  
415 of  $BC_{\text{solid}}$ . Liquid fuel combustion is the dominant source of BC in Nanjing,  
416 with 79% of BC generated from the consumption of liquid fuel. Interannually,  
417 the contributions of liquid fuel ranged from 76% to 81%, results that are  
418 comparable to other cities in China such as Wuhan (81%) and Shanghai (88-  
419 94%) (Zheng et al., 2020; Wei et al., 2020). The contribution of liquid fuel  
420 burning to BC was highest in summer (85%), in contrast to the lowest  
421 appeared in winter (72%), much higher than that of Beijing (35.7%) (Li et al.,  
422 2022). Beijing is heavily affected by heating activities in winter, such as  
423 power plants and residential heating using coal and biomass, resulting in  
424 higher solid fuel emissions. The seasonal average contribution of BB varied  
425 by 5%, from 19% to 24%, influenced by coal-fired emissions from  
426 surrounding factories and long-range transport of domestic cooking emissions  
427 in rural areas in the Yangtze River Delta region (Wei et al., 2020).



428

429 Figure 4 (A) Hourly variation of BC<sub>liquid</sub> and BC<sub>solid</sub>, and (B) their relative contribution to BC. The pie  
 430 charts in (A) are annual average relative contribution of BC<sub>liquid</sub> and BC<sub>solid</sub> to BC.

431 It is important to highlight that the results of the Aethalometer model are  
 432 highly dependent on the determination of AAE values, with AAE<sub>liquid</sub> ranges  
 433 between 0.8 to 1.1, and AAE<sub>solid</sub> values ranges between 1.8 to 2.2, as widely  
 434 used in this model (Helin et al., 2018; Dumka et al., 2019; Fuller et al., 2014).  
 435 To estimate the uncertainty of the Aethalometer model, we calculated source  
 436 apportionment results using different AAE pairs, the results are showed in  
 437 Table S1. The relative contributions of BC<sub>liquid</sub> and BC<sub>solid</sub> to BC ranged from  
 438 62% to 90% and 10% to 38%. Thus, an uncertainty estimation of 27.4% for  
 439 the Aethalometer model results in this work. Although there are uncertainties  
 440 in source apportionment results, our results indicate that liquid fuel  
 441 combustion is the main source of BC in Nanjing during the study period.

### 442 3.3.2 Source diagnostic tracers

443 The ratios of BC/PM<sub>2.5</sub> and BC/CO (carbon monoxide, CO) have been  
 444 utilized to estimate emission sources in previous studies since they can vary  
 445 when emitted from different sources (Chow et al., 2011; Zhang et al., 2009).  
 446 The proportion of BC in PM<sub>2.5</sub> is higher in traffic sources than that from other  
 447 sources (such as residential coal combustion and forest fire). As listed in Table  
 448 S2, higher BC/PM<sub>2.5</sub> ratios were found in heavy-duty diesel (33-74%) and





449 light-duty diesel (62-64%), followed by those from agricultural burning (6-  
450 13%) and forest fire (3%) (Table S2) (Chow et al., 2011). The highest ratio of  
451 BC/PM<sub>2.5</sub> appeared in autumn time (20%) while the lowest was observed in  
452 winter (8%), suggesting increased biomass and coal burning in winter.  
453 Previous studies reported that the ratio of BC/CO was lower in traffic  
454 emissions, as compared to the ratios from industry, power plant, residential  
455 and traffic emissions were 0.72%, 1.77%, 3.71%, and 0.52%, respectively  
456 (Table S2) (Zhang et al., 2009). The average ratios of BC/CO in spring,  
457 summer, autumn, and winter were 0.39%, 0.49%, 0.49%, and 0.31%,  
458 respectively, further suggesting that the traffic source was dominant in  
459 Nanjing (Table 3).

460 To further support the source apportionment results of BC, a correlation  
461 analysis was conducted between BC and trace gases such as SO<sub>2</sub>, and NO<sub>2</sub>,  
462 mainly derived from coal combustion, and vehicles emissions respectively.  
463 As listed in Table 3, the correlations of BC with NO<sub>2</sub> (0.54-0.67) were higher  
464 than the correlations of BC with SO<sub>2</sub> (0.16-0.59), further indicating the  
465 dominance of traffic emission in Nanjing.

466 Table 3 Mass ratios and correlations between BC and other pollutants

		Spring	Summer	Autumn	Winter	Annual
Mass ratios (%)	BC/PM <sub>2.5</sub>	12.93	10.63	19.64	7.92	12.78
	BC/CO	0.39	0.49	0.49	0.31	0.42
Correlation	BC-SO <sub>2</sub>	0.49	0.16	0.32	0.59	0.38
	BC-NO <sub>2</sub>	0.66	0.61	0.54	0.67	0.60

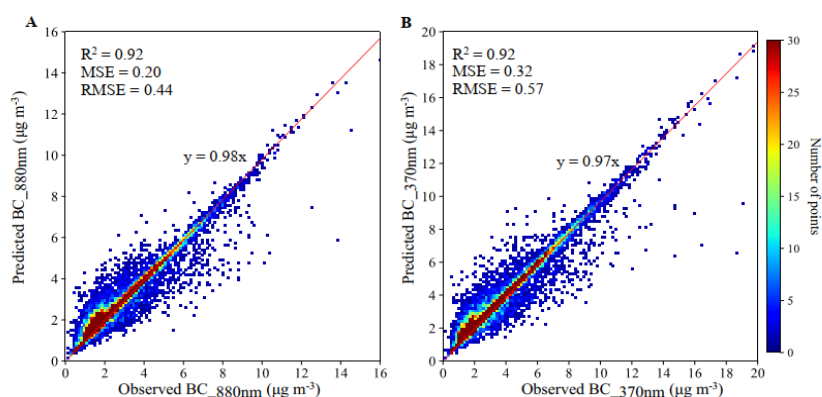
### 467 3.4 Long-term trend of BC

#### 468 3.4.1 Black carbon simulation results

469 After training the RF models with optimal hyperparameters, the models  
470 for BC at 880 nm and 370 nm were evaluated on test sets to assess  
471 predictive performance. The density scatter plot as displayed in Figure 5  
472 showed that the RF model accurately reproduced hourly BC concentrations at  
473 both wavelengths. The RF model explained over 90% of the variation in BC  
474 concentrations, achieving an R<sup>2</sup> of 0.92 between the monitored and predicted  
475 results at both 370 and 880 nm. At the 370 nm wavelength, the RMSE was  
476 0.57 μg m<sup>-3</sup>, which was 22.8% higher than the RMSE at 880 nm, likely due  
477 to the higher observed BC levels at this wavelength. In addition to evaluating



478 the RF model using the test set, further validation was conducted using  
479 Tracking Air Pollution in China (TAP) (10 km × 10 km, <http://tapdata.org.cn>)  
480 data. The predicted BC values at 880 nm from the RF model showed good  
481 agreement with the TAP dataset, with an R2 of 0.72 (Figure S5). Using the  
482 trained model and available predictors, hourly BC concentration at the  
483 sampling site can be accurately reconstructed for any given period, consistent  
484 with AE33.



485  
486 Figure 5 Density scatter plots of hourly observed and modeled BC at (a) 880 nm and (b) 370 nm

487 After training the RF models with input data, Shapley Additive  
488 exPlanations (SHAP) values were used to assess the importance of each  
489 predictors on model outcomes (Lundberg and Lee, 2017). Figure S6 presented  
490 the ranked average SHAP values for each predictor for BC at the two  
491 wavelengths. NO<sub>2</sub>, BLH and SO<sub>2</sub> were identified as having the greatest  
492 impact on model's prediction. Similar to BC, NO<sub>2</sub> and SO<sub>2</sub> are primarily  
493 emitted from incomplete combustion processes involving fossil fuels (Lee et  
494 al., 2017; Yao et al., 2002). As a result, BC, NO<sub>2</sub> and SO<sub>2</sub> are often co-emitted  
495 by factories or traffic near the sampling site. BLH determines the diffusion  
496 capacity of the atmosphere; a lower BLH means stronger atmospheric stability,  
497 resulting in increased BC levels on the surface air. Unlike BLH, the  
498 contribution of other meteorology predictors such as T, RH, WS and WD,  
499 were relatively low compared to pollutant gases. One possible reason for this  
500 is meteorological condition changes may not have an immediate effect on  
501 atmospheric BC levels; instead, there may be a certain lag in their effects.

### 502 3.4.2 Long-term temporal variation of BC

503 Meteorological data and air pollutants concentrations were used in the

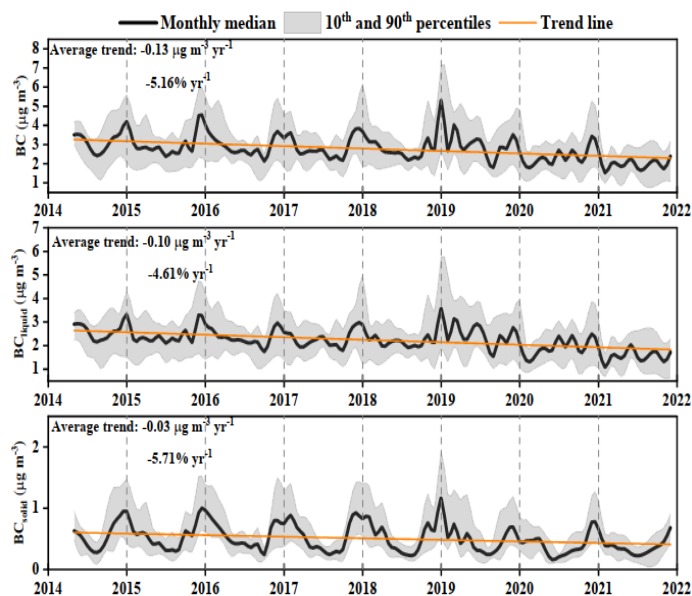


504 trained RF model to estimate BC concentrations at 370 and 880 nm from 2014  
505 to 2021. The Aethalometer Model, using AAE of 1 and 2, was then applied to  
506 the simulated BC to explore the long-term temporal variation of source-  
507 specific BC. Between 2014 and 2021, average BC concentrations decreased  
508 by 35.7% from  $3.12 \pm 1.39 \mu\text{g m}^{-3}$  in 2014 to  $2.04 \pm 0.33 \mu\text{g m}^{-3}$  in 2021. The  
509 statistical significance of the reduction in BC and source-specific BC was  
510 assessed using the Mann-Kendall test on monthly median values, with results  
511 shown in Figure 6. A significant decreasing trend ( $p < 0.01$ ) in BC  
512 concentrations was observed, with a slope of  $-0.13 \mu\text{g m}^{-3}\text{yr}^{-1}$ . Similar  
513 reductions have also been reported across various regions in China since 2013  
514 (He et al., 2023; Sun et al., 2022a; Chow et al., 2022; Dai et al., 2023).  
515 Significantly decreases were also observed in  $\text{BC}_{\text{liquid}}$  ( $p < 0.01$ ) and  $\text{BC}_{\text{solid}}$   
516 ( $p < 0.05$ ) concentrations. From 2014 to 2021,  $\text{BC}_{\text{liquid}}$ , decreased by 38.4%  
517 (from  $2.55 \pm 1.14 \mu\text{g m}^{-3}$  to  $1.57 \pm 0.89 \mu\text{g m}^{-3}$  in 2021) at an absolute rate of  
518  $-0.10 \mu\text{g m}^{-3}\text{yr}^{-1}$ , while  $\text{BC}_{\text{solid}}$  decreased by 20.3% (from  $0.59 \pm 0.52 \mu\text{g m}^{-3}$   
519 to  $0.47 \pm 0.33 \mu\text{g m}^{-3}$ ) at a rate of  $-0.03 \mu\text{g m}^{-3}\text{yr}^{-1}$ . The contributions of  
520 different sources to the overall BC reduction were estimated by comparing  
521 the absolute decrease slopes of  $\text{BC}_{\text{liquid}}$  and  $\text{BC}_{\text{solid}}$  to the overall BC decrease  
522 slope. It was found that 77 % of total BC reduction was due to the decreased  
523 liquid fuel combustion, highlighting the significant role of  $\text{BC}_{\text{liquid}}$  in reducing  
524 BC concentrations from 2014 to 2021.

525 Throughout the study period, BC concentrations exhibited two distinct  
526 decrease trends, aligned with the implementation of the Air Pollution and  
527 Control Action Plan (2013-2017, P1) and the Three-Year Action Plan (starting  
528 in 2018, P2) by the Chinese government. To compare the decreasing trends of  
529 BC in the two periods, the absolute trends were normalized by the average  
530 values for each period. The change rates of BC and other air pollutants are  
531 shown in Table 4. During P1, the relative slopes of BC and  $\text{BC}_{\text{liquid}}$  were -  
532  $4.18 \text{ \% yr}^{-1}$  ( $p < 0.1$ ) and  $-4.26 \text{ \% yr}^{-1}$  ( $p < 0.05$ ), respectively  $\text{BC}_{\text{liquid}}$   
533 accounted for 83% of the total decrease in atmospheric BC concentrations.  
534 Since the decrease in  $\text{BC}_{\text{solid}}$  is not significant, the actual contribution of  
535  $\text{BC}_{\text{liquid}}$  may be higher than estimated. Compared to P1, the decline in BC,  
536  $\text{BC}_{\text{liquid}}$  and  $\text{BC}_{\text{solid}}$  concentration during P2 was much steeper, reaching  $-10.9 \text{ \%}$   
537  $\text{yr}^{-1}$  ( $p < 0.01$ ),  $-9.7 \text{ \% yr}^{-1}$  ( $p < 0.01$ ) and  $-11.1 \text{ \% yr}^{-1}$  ( $p < 0.1$ ), respectively.  
538 In the S2 period, reductions in both  $\text{BC}_{\text{liquid}}$  and  $\text{BC}_{\text{solid}}$  contributed to the



539 overall decrease in BC concentration, with BC<sub>liquid</sub> still being the dominant  
 540 factor, accounting for 71% of the total reduction. SO<sub>2</sub> and NO<sub>2</sub>, which shared  
 541 the same sources as BC, also decreased more rapidly in S2 (-31.6 % yr<sup>-1</sup> and  
 542 -8.5 % yr<sup>-1</sup>) compared to S1 (-9.3 % yr<sup>-1</sup> and -0.7 % yr<sup>-1</sup>), suggesting that air  
 543 pollutants have been decreasing much faster after 2018 than before.



544  
 545 Figure 6 Trends in BC, BC<sub>liquid</sub> and BC<sub>solid</sub> at sampling site. The solid black line represents the monthly  
 546 medians, the dash black lines represent the 10th and 90th monthly percentiles, and the orange line is the  
 547 fitted long-term trend.

548 Table 4 The change rates of BC and other air pollutants during different period

Study Period	air pollutants	absolute slope <sup>a</sup>	relative slope <sup>b</sup>	<i>p</i>
Air Pollution	BC	-0.12	-4.18	0.10
	BC <sub>liquid</sub>	-0.10	-4.26	0.05
	BC <sub>solid</sub>	-0.02	-3.47	0.60
Prevention and Control Action Plan	PM <sub>2.5</sub>	-11.90	-25.28	0.01
	NO <sub>2</sub>	-0.29	-0.73	0.90
	SO <sub>2</sub>	-1.65	-9.34	0.10
	CO	0.01	1.10	0.77
After 2018	BC	-0.28	-10.85	0.01
	BC <sub>liquid</sub>	-0.20	-9.71	0.01
	BC <sub>solid</sub>	-0.05	-11.06	0.10
	PM <sub>2.5</sub>	-4.33	-14.96	0.05
	NO <sub>2</sub>	-3.06	-8.49	0.05

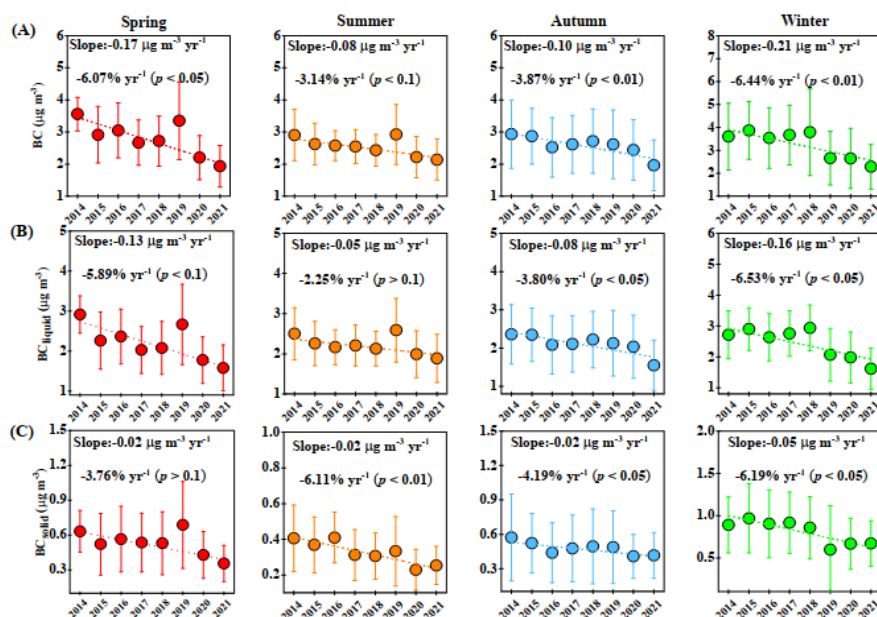


SO <sub>2</sub>	-2.36	-31.58	0.01
CO	0.02	2.73	0.64

549 <sup>a</sup>:  $\mu\text{g m}^{-3} \text{yr}^{-1}$

550 <sup>b</sup>: % yr<sup>-1</sup>

551 The seasonal trends in BC and its different sources were further  
552 investigated in Nanjing. As shown in Figure 7, significant reductions in BC  
553 concentrations were observed across all seasons. The decreasing slopes of BC  
554 in spring ( $-6.1\% \text{ yr}^{-1}$ ,  $p < 0.05$ ) and winter ( $-6.4\% \text{ yr}^{-1}$ ,  $p < 0.01$ ) were steeper  
555 than those in summer ( $-3.1\% \text{ yr}^{-1}$ ,  $p < 0.1$ ) and autumn ( $-3.9\% \text{ yr}^{-1}$ ,  $p < 0.01$ ).  
556 The reduction rate of PM<sub>2.5</sub> in spring ( $-18.9\% \text{ yr}^{-1}$ ,  $p < 0.05$ ), summer ( $-$   
557  $22.5\%$ ,  $p < 0.05$ ) and autumn ( $-15.9\% \text{ yr}^{-1}$ ,  $p < 0.1$ ) was 3 to 6 times that of  
558 BC (Table S3). In winter, the reduction rate ( $-9.8\% \text{ yr}^{-1}$ ,  $p < 0.01$ ) is closer  
559 to that of BC, suggesting that the reduction of primary pollutants in Nanjing  
560 during winter might be more effective compared to other seasons. The  
561 seasonal variation of BC<sub>liquid</sub> showed distinct trends across different seasons.  
562 Significant reductions were observed in spring, autumn and winter, with the  
563 absolute slope of  $-5.9\% \text{ yr}^{-1}$  ( $p < 0.1$ ),  $-3.8\% \text{ yr}^{-1}$  ( $p < 0.05$ ) and  $-6.5\% \text{ yr}^{-1}$   
564 ( $p < 0.05$ ), respectively. BC<sub>liquid</sub> in summer was not statistically significant,  
565 which may be partly due to increased traffic activity during tourism peak  
566 season, leading to higher liquid fuel consumption. Moreover, the reduction  
567 rate of PM<sub>2.5</sub> was faster in summer compared to BC, indicating that secondary  
568 aerosol reductions were more pronounced during this season. BC<sub>solid</sub> showed  
569 a similar decreasing slope in summer ( $-6.1\% \text{ yr}^{-1}$ ,  $p < 0.01$ ), and winter ( $-6.2\%$   
570  $\text{yr}^{-1}$ ,  $p < 0.05$ ), while autumn appeared relatively slower reduction ( $-4.2\% \text{ yr}^{-1}$   
571  $\text{yr}^{-1}$ ). Similar to BC<sub>solid</sub>, SO<sub>2</sub> exhibited a steeper change rate in winter ( $-24.4\%$   
572  $\text{yr}^{-1}$ ,  $p < 0.01$ ) and a slower change rate in autumn ( $-16.2\% \text{ yr}^{-1}$ ,  $p < 0.01$ )  
573 (Table S3). The reduction of BC<sub>solid</sub> in spring was not significant, which may  
574 be influenced by long-range transport of biomass burning, as well as increased  
575 agricultural activities during this season. It is worth noting that BC<sub>liquid</sub>  
576 contributed 76% to overall BC reduction in spring and BC<sub>solid</sub> contributed 25%  
577 to overall BC reduction in summer. However, since the decreasing trend of  
578 BC<sub>solid</sub> in spring and BC<sub>liquid</sub> in summer were not statistically significant, these  
579 contributions may have been underestimated.



580

581 Figure 7 Seasonal variation of (A) BC, (B) BC<sub>liquid</sub> and (C) BC<sub>solid</sub> in spring, summer, autumn and  
 582 winter. The circle in different color represents the average concentration of BC, BC<sub>liquid</sub> and BC<sub>solid</sub>. The  
 583 vertical lines represent the standard deviations of BC, BC<sub>liquid</sub> and BC<sub>solid</sub>.

### 584 3.4.3 The impact of Emission and Meteorology

585 In addition to changes in emissions, meteorological conditions can also  
 586 affect the long-term trends of pollutants by influencing their long-range  
 587 transport and processes of dry and wet deposition. To explore these impacts  
 588 on the long-term trends of BC, the KZ filter was applied to distinguish  
 589 between emission-related ( $E_{LT}^{emi}$ ) and meteorology-related ( $E_{LT}^{met}$ ) trends. The  
 590 daily averaged log-transformed original time series along with decoupled  
 591 short-term, baseline and seasonal of BC were described in Figure S7. The  
 592 short-term component of BC displayed notable fluctuations, while the  
 593 seasonal component showed a clear cycle with higher levels in winter and  
 594 lower levels in summer. The largest variances for BC (69%), BC<sub>liquid</sub> (73%)  
 595 and BC<sub>solid</sub> (52%) were found in short-term component, reflecting the  
 596 essential role of synoptic weather on the daily variations of primary aerosol  
 597 content in Nanjing (Table S4). BC<sub>solid</sub> exhibits seasonal dependence with  
 598 relatively higher seasonal component (40%) than BC (16%) and BC<sub>liquid</sub>  
 599 (12%). The sum of variances explained by the short-term, seasonal and long-



600 term component for BC, BC<sub>liquid</sub> and BC<sub>solid</sub> were 93%, 92% and 92%,  
601 respectively. A total variance close to 100% indicating that these three  
602 components are largely independent of each other, suggesting that most of  
603 the meteorological influence have been effectively accounted and removed  
604 (Chen et al., 2019; Sun et al., 2022b; Zheng et al., 2020). To separate  
605 emission-related ( $E_{LT}^{emi}$ ) and meteorology-related components ( $E_{LT}^{met}$ ) from the  
606 long-term component ( $E_{LT}$ ), multiple linear regression was conducted using  
607 the baseline component of meteorological parameters and BC. The model  
608 incorporating these meteorological parameters accurately reproduced the  
609 baseline of BC<sub>solid</sub> ( $R^2 = 0.84, p < 0.001$ ). In contrast, it was less effective in  
610 explaining the baseline for BC ( $R^2 = 0.59, p < 0.001$ ) and BC<sub>liquid</sub> ( $R^2 = 0.51,$   
611  $p < 0.001$ ), suggesting that local emission changes across different seasons  
612 play an important role in impacting BC and BC<sub>liquid</sub> in Nanjing.

613 The linear trends of  $E_{LT}$ ,  $E_{LT}^{emi}$  and  $E_{LT}^{met}$  for BC, BC<sub>liquid</sub> and BC<sub>solid</sub> are  
614 summarized in Table 5. It is important to note that the linear trend slope of  
615  $E_{LT}$  represents relative change rate (% yr<sup>-1</sup>) of the baseline concentration,  
616 since original time series of BC were log-transformed before applying the KZ  
617 filter. To convert the fractional change rate into an absolute change rate ( $\mu\text{g}$   
618  $\text{m}^{-3} \text{yr}^{-1}$ ), it is multiplied by the average baseline concentration (not log-  
619 transformed). The  $E_{LT}$  of BC and its distinct source exhibited significant ( $p <$   
620  $0.01$ ) declining trends, with slopes of -0.1, -0.08 and -0.02  $\mu\text{g m}^{-3} \text{yr}^{-1}$  for BC,  
621 BC<sub>liquid</sub> and BC<sub>solid</sub>, respectively. BC<sub>liquid</sub> was the dominant contributor to BC  
622 reduction, accounting for 80% of the overall decrease, suggesting that when  
623 the influence of seasonal and synoptic variations is excluded, its contribution  
624 to BC temporal variations becomes more evident. In addition, the relative  
625 contributions of  $E_{LT}^{emi}$  and  $E_{LT}^{met}$  to BC reduction were quantified by calculating  
626 the ratio of their absolute slopes to that of  $E_{LT}$  (Zheng et al., 2023). Both  
627 meteorology conditions and emission reductions played crucial roles in  
628 reducing BC and its specific sources. Emission reductions were found to be  
629 the major contributor to the decline in long-term trends of BC, BC<sub>liquid</sub> and  
630 BC<sub>solid</sub>, with contributions of 70%, 63% and 86%, respectively. While  
631 emissions reductions dominated the decrease in BC concentrations  
632 throughout the study period, their relative influence compared to  
633 meteorological conditions varied between the P1 (before 2018) and P2 (after  
634 2018) phases. As shown in Figure 8, emission reductions played a more



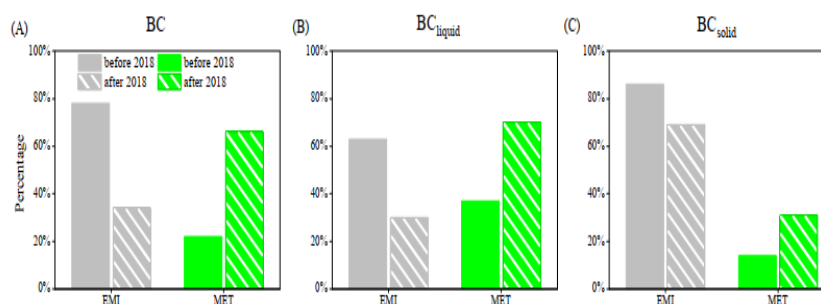
635 prominent role, contributing 78%, 62% and 86% to the reductions in BC,  
 636 BC<sub>liquid</sub> and BC<sub>solid</sub>, respectively. However, during P2, meteorological  
 637 conditions played a leading role in reducing BC and BC<sub>liquid</sub>, contributing 66%  
 638 and 70%, respectively. Moreover, meteorology condition had a notable  
 639 impact on BC<sub>solid</sub> in P2, with its contribution increasing from 14% in P1 to  
 640 31%. This suggests that the rapid reduction of BC in P2 was largely due to  
 641 favorable meteorological conditions, which played a crucial role in  
 642 facilitating its decline.

643 Table 5 Linear trends of long-term component of BC and its sources including BC<sub>liquid</sub> and BC<sub>solid</sub>

Components	BC			BC <sub>liquid</sub>			BC <sub>solid</sub>		
	absolute <sup>a</sup>	relative <sup>b</sup>	<i>p</i>	absolute <sup>a</sup>	relative <sup>b</sup>	<i>p</i>	absolute <sup>a</sup>	relative <sup>b</sup>	<i>p</i>
E <sub>LT</sub>	-0.10	-3.76	0.01	-0.08	-3.54	0.01	-0.014	-4.91	0.01
E <sub>LT</sub> <sup>EMI</sup>	-0.07	-2.63	0.01	-0.05	-2.20	0.01	-0.012	-3.62	0.01
E <sub>LT</sub> <sup>MET</sup>	-0.03	-1.13	0.01	-0.03	-1.32	0.01	-0.002	-1.27	0.01

644 <sup>a</sup>:  $\mu\text{g m}^{-3} \text{ yr}^{-1}$

645 <sup>b</sup>: % yr<sup>-1</sup>



646

647 Figure 8 Contributions of Emission Reduction Policies and Meteorological Conditions to the  
 648 Decrease in BC Concentrations Before and After 2018. The (A), (B) and (C) panels represent BC,  
 649 BC<sub>liquid</sub> and BC<sub>solid</sub>.

#### 650 4. Conclusion

651 In this work, BC mass concentrations were continuously monitored in  
 652 Nanjing, China, from 2019 to 2021. Combining observations with random  
 653 forest algorithm, the BC concentrations from 2014-2021 were reconstructed  
 654 to explore the long-term trends of BC and its sources during two distinct  
 655 emission reduction periods. The results showed that BC concentrations were  
 656 analyzed to reveal its characteristics and sources. The annual average BC  
 657 mass concentration during the study period was  $2.5 \pm 1.6 \mu\text{g m}^{-3}$ . Relatively





658 higher BC mass concentrations were found in winter, while no clear variation  
659 was observed during other seasons, implying a locally dominant BC source.  
660 Diurnal variations showed a bimodal pattern with lower concentrations in  
661 daytime and higher values in night, primarily influenced by traffic rush hours  
662 and boundary layer heights. Liquid fuel combustion contributed more than 75%  
663 to BC in all years, with the highest contribution appearing in summer (85%)  
664 and the lowest in winter (72%).

665 The RF models explained over 90% variation and accurately captured  
666 seasonal cycle well of BC at 880 nm, demonstrating the strong predictive  
667 capability of the trained models. The long-term trend of BC,  $BC_{\text{liquid}}$  and  
668  $BC_{\text{solid}}$  all exhibited significant ( $p < 0.05$ ) declines, with  $BC_{\text{liquid}}$  contributing  
669 the most to the overall BC reduction, accounting for 77% of the total decrease  
670 over entire period. Notably, BC levels decreased most rapidly during winter,  
671 while the reduction in summer was much slower. The trend in BC reduction  
672 varied between two distinct phases, in P2 (after 2018), BC levels declined  
673 much steeper compared to that in P1 (2014-2017), indicating that policies  
674 aimed at replacing coal to cleaner energy have been particularly effective in  
675 reducing primary pollutants. Over the entire period, emission reduction was  
676 the primary driver of BC reduction, contributing to BC,  $BC_{\text{liquid}}$  and  $BC_{\text{solid}}$   
677 reduction, with contribution of 70%, 63%, and 86%, respectively while  
678 meteorological conditions accounted for 30%, 37% and 24%. Although  
679 emission reduction dominated BC reduction over the entire period, the  
680 contributions of emission reduction and meteorological conditions to BC  
681 reduction differed between the two phases. In P1, emission reduction played  
682 a dominant role, while in P2, meteorological conditions became the primary  
683 driver of BC reduction. Our results highlight that to further reduce  
684 atmospheric BC, targeted policies should be implemented to restrict liquid  
685 fuel combustion, especially during the summer. Additionally, the impact of  
686 meteorological factors on BC concentrations should not be overlooked during  
687 emission reduction efforts.

#### 688 **Data Availability**

689 The hourly meteorological reanalysis data ERA5 are available in the ECMWF  
690 at [https://cds.climate.copernicus.eu/cdsapp#!/dataset/reanalysis-era5-single-](https://cds.climate.copernicus.eu/cdsapp#!/dataset/reanalysis-era5-single-levels?tab=form)  
691 [levels?tab=form](https://cds.climate.copernicus.eu/cdsapp#!/dataset/reanalysis-era5-single-levels?tab=form). Hourly averaged concentrations of  $PM_{2.5}$ , CO,  $SO_2$  and  $NO_2$   
692 were obtained from <https://quotsoft.net/air/>. All the observational and



693 predicted data were openly accessible at the Open Science Framework  
694 <https://osf.io/8n32t/>.

#### 695 **Competing interests**

696 The contact author has declared that none of the authors has any competing  
697 interests.

#### 698 **Author contributions**

699 Yanlin Zhang designed the research. Fang Cao, Mingyuan Yu, and Chaman  
700 Gul took part in data analysis and revised and commented on the paper.  
701 Abudurexiati·Abulimiti wrote the paper. Yihang Hong analysis the data. All  
702 authors contributed to the discussion of this paper.

#### 703 **Acknowledgement**

704 This research was financially supported by the National Natural Science  
705 Foundation of China (No. 42192512, 42107123, 42273087).

#### 706 **References**

- 707 Bauwens, M., Compernelle, S., Stavrakou, T., Müller, J.-F., van Gent, J., Eskes, H., Levelt, P. F., van  
708 der A, R., Veefkind, J. P., Vlietinck, J., Yu, H., and Zehner, C.: Impact of Coronavirus Outbreak on  
709 NO<sub>2</sub> Pollution Assessed Using TROPOMI and OMI Observations, *Geophysical Research Letters*, 47,  
710 e2020GL087978, <https://doi.org/10.1029/2020GL087978>, 2020.
- 711 Bond, T. C., Doherty, S. J., Fahey, D. W., Forster, P. M., Berntsen, T., DeAngelo, B. J., Flanner, M. G.,  
712 Ghan, S., Kärcher, B., Koch, D., Kinne, S., Kondo, Y., Quinn, P. K., Sarofim, M. C., Schultz, M. G.,  
713 Schulz, M., Venkataraman, C., Zhang, H., Zhang, S., Bellouin, N., Guttikunda, S. K., Hopke, P. K.,  
714 Jacobson, M. Z., Kaiser, J. W., Klimont, Z., Lohmann, U., Schwarz, J. P., Shindell, D., Storelvmo, T.,  
715 Warren, S. G., and Zender, C. S.: Bounding the role of black carbon in the climate system: A  
716 scientific assessment, *Journal of Geophysical Research: Atmospheres*, 118, 5380-5552,  
717 <https://doi.org/10.1002/jgrd.50171>, 2013.
- 718 Cao, J. J., Zhu, C. S., Chow, J. C., Watson, J. G., Han, Y. M., Wang, G. h., Shen, Z. x., and An, Z. S.:  
719 Black carbon relationships with emissions and meteorology in Xi'an, China, *Atmospheric Research*,  
720 94, 194-202, <https://doi.org/10.1016/j.atmosres.2009.05.009>, 2009.
- 721 Chang, Y., Deng, C., Cao, F., Cao, C., Zou, Z., Liu, S., Lee, X., Li, J., Zhang, G., and Zhang, Y.:  
722 Assessment of carbonaceous aerosols in Shanghai, China – Part 1: long-term evolution, seasonal  
723 variations, and meteorological effects, *Atmos. Chem. Phys.*, 17, 9945-9964, 10.5194/acp-17-  
724 9945-2017, 2017.
- 725 Chen, Z., Chen, D., Kwan, M. P., Chen, B., Gao, B., Zhuang, Y., Li, R., and Xu, B.: The control of  
726 anthropogenic emissions contributed to 80% of the decrease in PM<sub>2.5</sub> concentrations in  
727 Beijing from 2013 to 2017, *Atmos. Chem. Phys.*, 19, 13519-13533, 10.5194/acp-19-13519-2019,  
728 2019.
- 729 Cheng, J., Su, J., Cui, T., Li, X., Dong, X., Sun, F., Yang, Y., Tong, D., Zheng, Y., Li, Y., Li, J., Zhang, Q.,  
730 and He, K.: Dominant role of emission reduction in PM<sub>2.5</sub> air quality improvement in Beijing during  
731 2013–2017: a model-based decomposition analysis, *Atmos. Chem. Phys.*, 19, 6125-6146,  
732 10.5194/acp-19-6125-2019, 2019.



- 733 Chow, J. C., Watson, J. G., Lowenthal, D. H., Antony Chen, L. W., and Motallebi, N.: PM<sub>2.5</sub> source  
734 profiles for black and organic carbon emission inventories, *Atmospheric Environment*, 45, 5407–  
735 5414, <https://doi.org/10.1016/j.atmosenv.2011.07.011>, 2011.
- 736 Chow, W. S., Liao, K., Huang, X. H. H., Leung, K. F., Lau, A. K. H., and Yu, J. Z.: Measurement report:  
737 The 10-year trend of PM<sub>2.5</sub> major components and source tracers from 2008 to 2017 in an urban  
738 site of Hong Kong, China, *Atmos. Chem. Phys.*, 22, 11557–11577, 10.5194/acp-22-11557-2022,  
739 2022.
- 740 Dai, M., Zhu, B., Fang, C., Zhou, S., Lu, W., Zhao, D., Ding, D., Pan, C., and Liao, H.: Long-Term  
741 Variation and Source Apportionment of Black Carbon at Mt. Waliguan, China, *Journal of*  
742 *Geophysical Research: Atmospheres*, 126, e2021JD035273,  
743 <https://doi.org/10.1029/2021JD035273>, 2021.
- 744 Dai, T., Dai, Q., Ding, J., Liu, B., Bi, X., Wu, J., Zhang, Y., and Feng, Y.: Measuring the Emission  
745 Changes and Meteorological Dependence of Source-Specific BC Aerosol Using Factor Analysis  
746 Coupled With Machine Learning, *Journal of Geophysical Research: Atmospheres*, 128,  
747 e2023JD038696, <https://doi.org/10.1029/2023JD038696>, 2023.
- 748 Ding, A. J., Huang, X., Nie, W., Sun, J. N., Kerminen, V.-M., Petäjä, T., Su, H., Cheng, Y. F., Yang, X.-  
749 Q., Wang, M. H., Chi, X. G., Wang, J. P., Virkkula, A., Guo, W. D., Yuan, J., Wang, S. Y., Zhang, R. J.,  
750 Wu, Y. F., Song, Y., Zhu, T., Zilitinkevich, S., Kulmala, M., and Fu, C. B.: Enhanced haze pollution by  
751 black carbon in megacities in China, *Geophysical Research Letters*, 43, 2873–2879,  
752 <https://doi.org/10.1002/2016GL067745>, 2016.
- 753 Drinovec, L., Močnik, G., Zotter, P., Prévôt, A. S. H., Ruckstuhl, C., Coz, E., Rupakheti, M., Sciare, J.,  
754 Müller, T., Wiedensohler, A., and Hansen, A. D. A.: The "dual-spot" Aethalometer: an improved  
755 measurement of aerosol black carbon with real-time loading compensation, *Atmos. Meas. Tech.*,  
756 8, 1965–1979, 10.5194/amt-8-1965-2015, 2015.
- 757 Du, H., Li, J., Wang, Z., Chen, X., Yang, W., Sun, Y., Xin, J., Pan, X., Wang, W., Ye, Q., and Dao, X.:  
758 Assessment of the effect of meteorological and emission variations on winter PM<sub>2.5</sub> over the North  
759 China Plain in the three-year action plan against air pollution in 2018–2020, *Atmospheric Research*,  
760 280, 106395, <https://doi.org/10.1016/j.atmosres.2022.106395>, 2022.
- 761 Dumka, U. C., Kaskaoutis, D. G., Devara, P. C. S., Kumar, R., Kumar, S., Tiwari, S., Gerasopoulos, E.,  
762 and Mihalopoulos, N.: Year-long variability of the fossil fuel and wood burning black carbon  
763 components at a rural site in southern Delhi outskirts, *Atmospheric Research*, 216, 11–25,  
764 <https://doi.org/10.1016/j.atmosres.2018.09.016>, 2019.
- 765 Fan, M.-Y., Hong, Y., Zhang, Y.-L., Sha, T., Lin, Y.-C., Cao, F., and Guo, H.: Increasing Nonfossil Fuel  
766 Contributions to Atmospheric Nitrate in Urban China from Observation to Prediction,  
767 *Environmental Science & Technology*, 57, 18172–18182, 10.1021/acs.est.3c01651, 2023.
- 768 Fuller, G. W., Tremper, A. H., Baker, T. D., Yttri, K. E., and Butterfield, D.: Contribution of wood  
769 burning to PM<sub>10</sub> in London, *Atmospheric Environment*, 87, 87–94,  
770 <https://doi.org/10.1016/j.atmosenv.2013.12.037>, 2014.
- 771 Grange, S. K., Carslaw, D. C., Lewis, A. C., Boleti, E., and Hueglin, C.: Random forest meteorological  
772 normalisation models for Swiss PM<sub>10</sub> trend analysis, *Atmos. Chem. Phys.*, 18, 6223–6239,  
773 10.5194/acp-18-6223-2018, 2018.
- 774 Gul, C., Mahapatra, P. S., Kang, S., Singh, P. K., Wu, X., He, C., Kumar, R., Rai, M., Xu, Y., and Puppala,  
775 S. P.: Black carbon concentration in the central Himalayas: Impact on glacier melt and potential



776 source contribution, Environmental Pollution, 275, 116544,  
777 <https://doi.org/10.1016/j.envpol.2021.116544>, 2021.

778 He, C., Niu, X., Ye, Z., Wu, Q., Liu, L., Zhao, Y., Ni, J., Li, B., and Jin, J.: Black carbon pollution in China  
779 from 2001 to 2019: Patterns, trends, and drivers, Environmental Pollution, 324, 121381,  
780 <https://doi.org/10.1016/j.envpol.2023.121381>, 2023.

781 Helin, A., Niemi, J. V., Virkkula, A., Pirjola, L., Teinilä, K., Backman, J., Aurela, M., Saarikoski, S., Rönkkö,  
782 T., Asmi, E., and Timonen, H.: Characteristics and source apportionment of black carbon in the  
783 Helsinki metropolitan area, Finland, Atmospheric Environment, 190, 87–98,  
784 <https://doi.org/10.1016/j.atmosenv.2018.07.022>, 2018.

785 Hong, Y., Zhang, Y., Bao, M., Fan, M., Lin, Y. C., Xu, R., Shu, Z., Wu, J. Y., Cao, F., Jiang, H., Cheng,  
786 Z., Li, J., and Zhang, G.: Nitrogen - Containing Functional Groups Dominate the Molecular  
787 Absorption of Water-Soluble Humic-Like Substances in Air From Nanjing, China Revealed by the  
788 Machine Learning Combined FT - ICR - MS Technique, Journal of Geophysical Research:  
789 Atmospheres, 128, 10.1029/2023JD039459, 2023.

790 Huang, Z.-J., Li, H., Luo, J.-Y., Li, S., and Liu, F.: Few-Shot Learning-Based, Long-Term Stable,  
791 Sensitive Chemosensor for On-Site Colorimetric Detection of Cr(VI), Analytical Chemistry, 95,  
792 6156–6162, 10.1021/acs.analchem.3c00604, 2023.

793 IPCC: Climate Change 2022 – Impacts, Adaptation and Vulnerability: Working Group II  
794 Contribution to the Sixth Assessment Report of the Intergovernmental Panel on Climate Change,  
795 Cambridge University Press, Cambridge, 10.1017/9781009325844, 2023.

796 Jiang, X., Li, G., and Fu, W.: Government environmental governance, structural adjustment and air  
797 quality: A quasi-natural experiment based on the Three-year Action Plan to Win the Blue Sky  
798 Defense War, Journal of Environmental Management, 277, 111470,  
799 <https://doi.org/10.1016/j.jenvman.2020.111470>, 2021.

800 Lee, B. P., Louie, P. K. K., Luk, C., and Chan, C. K.: Evaluation of traffic exhaust contributions to  
801 ambient carbonaceous submicron particulate matter in an urban roadside environment in Hong  
802 Kong, Atmos. Chem. Phys., 17, 15121–15135, 10.5194/acp-17-15121-2017, 2017.

803 Li, L., Li, Q., Huang, L., Wang, Q., Zhu, A., Xu, J., Liu, Z., Li, H., Shi, L., Li, R., Azari, M., Wang, Y.,  
804 Zhang, X., Liu, Z., Zhu, Y., Zhang, K., Xue, S., Ooi, M. C. G., Zhang, D., and Chan, A.: Air quality  
805 changes during the COVID-19 lockdown over the Yangtze River Delta Region: An insight into the  
806 impact of human activity pattern changes on air pollution variation, Science of The Total  
807 Environment, 732, 139282, <https://doi.org/10.1016/j.scitotenv.2020.139282>, 2020.

808 Li, R., Han, Y., Wang, L., Shang, Y., and Chen, Y.: Differences in oxidative potential of black carbon  
809 from three combustion emission sources in China, Journal of Environmental Management, 240,  
810 57–65, <https://doi.org/10.1016/j.jenvman.2019.03.070>, 2019.

811 Li, W., Liu, X., Duan, F., Qu, Y., and An, J.: A one-year study on black carbon in urban Beijing:  
812 Concentrations, sources and implications on visibility, Atmospheric Pollution Research, 13, 101307,  
813 <https://doi.org/10.1016/j.apr.2021.101307>, 2022.

814 Li, Y., Lei, L., Sun, J., Gao, Y., Wang, P., Wang, S., Zhang, Z., Du, A., Li, Z., Wang, Z., Kim, J. Y., Kim,  
815 H., Zhang, H., and Sun, Y.: Significant Reductions in Secondary Aerosols after the Three-Year  
816 Action Plan in Beijing Summer, Environmental Science & Technology, 57, 15945–15955,  
817 10.1021/acs.est.3c02417, 2023.

818 Lin, Y.-C., Zhang, Y.-L., Xie, F., Fan, M.-Y., and Liu, X.: Substantial decreases of light absorption,



819 concentrations and relative contributions of fossil fuel to light-absorbing carbonaceous aerosols  
820 attributed to the COVID-19 lockdown in east China, *Environmental Pollution*, 275, 116615,  
821 <https://doi.org/10.1016/j.envpol.2021.116615>, 2021.

822 Liu, D., He, C., Schwarz, J. P., and Wang, X.: Lifecycle of light-absorbing carbonaceous aerosols in  
823 the atmosphere, *npj Climate and Atmospheric Science*, 3, 40, 10.1038/s41612-020-00145-8, 2020.

824 Liu, Y., Yan, C., and Zheng, M.: Source apportionment of black carbon during winter in Beijing,  
825 *Science of The Total Environment*, 618, 531-541, <https://doi.org/10.1016/j.scitotenv.2017.11.053>,  
826 2018.

827 Lundberg, S. M. and Lee, S.-I.: A unified approach to interpreting model predictions, *Advances in*  
828 *neural information processing systems*, 30, 2017.

829 Qin, Y., Ye, J., Ohno, P., Liu, P., Wang, J., Fu, P., Zhou, L., Li, Y. J., Martin, S. T., and Chan, C. K.:  
830 Assessing the Nonlinear Effect of Atmospheric Variables on Primary and Oxygenated Organic  
831 Aerosol Concentration Using Machine Learning, *ACS Earth and Space Chemistry*, 6, 1059-1066,  
832 10.1021/acsearthspacechem.1c00443, 2022.

833 Ramanathan, V. and Carmichael, G.: Global and regional climate changes due to black carbon,  
834 *Nature Geoscience*, 1, 221-227, 10.1038/ngeo156, 2008.

835 Ran, L., Deng, Z. Z., Wang, P. C., and Xia, X. A.: Black carbon and wavelength-dependent aerosol  
836 absorption in the North China Plain based on two-year aethalometer measurements, *Atmospheric*  
837 *Environment*, 142, 132-144, <https://doi.org/10.1016/j.atmosenv.2016.07.014>, 2016.

838 Sandradewi, J., Prévôt, A. S. H., Szidat, S., Perron, N., Alfarra, M. R., Lanz, V. A., Weingartner, E., and  
839 Baltensperger, U.: Using Aerosol Light Absorption Measurements for the Quantitative  
840 Determination of Wood Burning and Traffic Emission Contributions to Particulate Matter,  
841 *Environmental Science & Technology*, 42, 3316-3323, 10.1021/es702253m, 2008.

842 Sarigiannis, D., Karakitsios, S. P., Zikopoulos, D., Nikolaki, S., and Kermenidou, M.: Lung cancer risk  
843 from PAHs emitted from biomass combustion, *Environ Res*, 137, 147-156,  
844 10.1016/j.envres.2014.12.009, 2015.

845 Seo, J., Park, D. S. R., Kim, J. Y., Youn, D., Lim, Y. B., and Kim, Y.: Effects of meteorology and emissions  
846 on urban air quality: a quantitative statistical approach to long-term records (1999-2016) in Seoul,  
847 South Korea, *Atmos. Chem. Phys.*, 18, 16121-16137, 10.5194/acp-18-16121-2018, 2018.

848 Sun, J., Wang, Z., Zhou, W., Xie, C., Wu, C., Chen, C., Han, T., Wang, Q., Li, Z., Li, J., Fu, P., Wang, Z.,  
849 and Sun, Y.: Measurement report: Long-term changes in black carbon and aerosol optical  
850 properties from 2012 to 2020 in Beijing, China, *Atmos. Chem. Phys.*, 22, 561-575, 10.5194/acp-  
851 22-561-2022, 2022a.

852 Sun, X., Zhao, T., Bai, Y., Kong, S., Zheng, H., Hu, W., Ma, X., and Xiong, J.: Meteorology impact on  
853 PM<sub>2.5</sub> change over a receptor region in the regional transport of air pollutants: observational  
854 study of recent emission reductions in central China, *Atmos. Chem. Phys.*, 22, 3579-3593,  
855 10.5194/acp-22-3579-2022, 2022b.

856 Wang, Y., Yuan, Y., Wang, Q., Liu, C., Zhi, Q., and Cao, J.: Changes in air quality related to the  
857 control of coronavirus in China: Implications for traffic and industrial emissions, *Science of The*  
858 *Total Environment*, 731, 139133, <https://doi.org/10.1016/j.scitotenv.2020.139133>, 2020.

859 Wei, C., Wang, M. H., Fu, Q. Y., Dai, C., Huang, R., and Bao, Q.: Temporal Characteristics and  
860 Potential Sources of Black Carbon in Megacity Shanghai, China, *Journal of Geophysical Research:*  
861 *Atmospheres*, 125, e2019JD031827, <https://doi.org/10.1029/2019JD031827>, 2020.



862 Wise, E. K. and Comrie, A. C.: Extending the Kolmogorov–Zurbenko Filter: Application to Ozone,  
863 Particulate Matter, and Meteorological Trends, *Journal of the Air & Waste Management*  
864 *Association*, 55, 1208–1216, 10.1080/10473289.2005.10464718, 2005.

865 Wu, B., Wu, C., Ye, Y., Pei, C., Deng, T., Li, Y. J., Lu, X., Wang, L., Hu, B., Li, M., and Wu, D.: Long-  
866 term hourly air quality data bridging of neighboring sites using automated machine learning: A  
867 case study in the Greater Bay area of China, *Atmospheric Environment*, 321, 120347,  
868 <https://doi.org/10.1016/j.atmosenv.2024.120347>, 2024.

869 Xiao, S., Yu, X., Zhu, B., Kumar, K. R., Li, M., and Li, L.: Characterization and source apportionment  
870 of black carbon aerosol in the Nanjing Jiangbei New Area based on two years of measurements  
871 from Aethalometer, *Journal of Aerosol Science*, 139, 105461,  
872 <https://doi.org/10.1016/j.jaerosci.2019.105461>, 2020.

873 Yao, X., Chan, C. K., Fang, M., Cadle, S., Chan, T., Mulawa, P., He, K., and Ye, B.: The water-soluble  
874 ionic composition of PM<sub>2.5</sub> in Shanghai and Beijing, China, *Atmospheric Environment*, 36, 4223–  
875 4234, [https://doi.org/10.1016/S1352-2310\(02\)00342-4](https://doi.org/10.1016/S1352-2310(02)00342-4), 2002.

876 Yin, C., Deng, X., Zou, Y., Solmon, F., Li, F., and Deng, T.: Trend analysis of surface ozone at  
877 suburban Guangzhou, China, *Science of The Total Environment*, 695, 133880,  
878 <https://doi.org/10.1016/j.scitotenv.2019.133880>, 2019.

879 Yu, M., Zhang, Y.-L., Xie, T., Song, W., Lin, Y.-C., Zhang, Y., Cao, F., Yang, C., and Szidat, S.:  
880 Quantification of fossil and non-fossil sources to the reduction of carbonaceous aerosols in the  
881 Yangtze River Delta, China: Insights from radiocarbon analysis during 2014–2019, *Atmospheric*  
882 *Environment*, 292, 119421, <https://doi.org/10.1016/j.atmosenv.2022.119421>, 2023.

883 Zhang, L., Shen, F., Gao, J., Cui, S., Yue, H., Wang, J., Chen, M., and Ge, X.: Characteristics and  
884 potential sources of black carbon particles in suburban Nanjing, China, *Atmospheric Pollution*  
885 *Research*, 11, 981–991, <https://doi.org/10.1016/j.apr.2020.02.011>, 2020.

886 Zhang, Q., Streets, D. G., Carmichael, G. R., He, K. B., Huo, H., Kannari, A., Klimont, Z., Park, I. S.,  
887 Reddy, S., Fu, J. S., Chen, D., Duan, L., Lei, Y., Wang, L. T., and Yao, Z. L.: Asian emissions in 2006  
888 for the NASA INTEX-B mission, *Atmos. Chem. Phys.*, 9, 5131–5153, 10.5194/acp-9-5131-2009,  
889 2009.

890 Zhang, Q., Zheng, Y., Tong, D., Shao, M., Wang, S., Zhang, Y., Xu, X., Wang, J., He, H., Liu, W., Ding,  
891 Y., Lei, Y., Li, J., Wang, Z., Zhang, X., Wang, Y., Cheng, J., Liu, Y., Shi, Q., Yan, L., Geng, G., Hong, C.,  
892 Li, M., Liu, F., Zheng, B., Cao, J., Ding, A., Gao, J., Fu, Q., Huo, J., Liu, B., Liu, Z., Yang, F., He, K., and  
893 Hao, J.: Drivers of improved PM<sub>2.5</sub> air quality in China from 2013 to 2017,  
894 *Proceedings of the National Academy of Sciences*, 116, 24463–24469,  
895 doi:10.1073/pnas.1907956116, 2019.

896 Zhang, X., Rao, R., Huang, Y., Mao, M., Berg, M. J., and Sun, W.: Black carbon aerosols in urban  
897 central China, *Journal of Quantitative Spectroscopy and Radiative Transfer*, 150, 3–11,  
898 <https://doi.org/10.1016/j.jqsrt.2014.03.006>, 2015.

899 Zhang, Y.-L., Li, J., Zhang, G., Zotter, P., Huang, R.-J., Tang, J.-H., Wacker, L., Prévôt, A. S. H., and  
900 Szidat, S.: Radiocarbon-Based Source Apportionment of Carbonaceous Aerosols at a Regional  
901 Background Site on Hainan Island, South China, *Environmental Science & Technology*, 48, 2651–  
902 2659, 10.1021/es4050852, 2014.

903 Zhao, C., Wang, Q., Ban, J., Liu, Z., Zhang, Y., Ma, R., Li, S., and Li, T.: Estimating the daily PM<sub>2.5</sub>  
904 concentration in the Beijing–Tianjin–Hebei region using a random forest model with a 0.01° × 0.01°



905 spatial resolution, *Environment International*, 134, 105297,  
906 <https://doi.org/10.1016/j.envint.2019.105297>, 2020.

907 Zheng, H., Kong, S., Zhai, S., Sun, X., Cheng, Y., Yao, L., Song, C., Zheng, Z., Shi, Z., and Harrison, R.  
908 M.: An intercomparison of weather normalization of PM<sub>2.5</sub> concentration using traditional  
909 statistical methods, machine learning, and chemistry transport models, *npj Climate and  
910 Atmospheric Science*, 6, 214, 10.1038/s41612-023-00536-7, 2023.

911 Zheng, H., Kong, S. F., Zheng, M. M., Yan, Y., Yao, L., Zheng, S., Yan, Q., Wu, J., Cheng, Y., Chen, N.,  
912 Bai, Y., Zhao, T., Liu, D., Zhao, D., and Qi, S.: A 5.5-year observations of black carbon aerosol at a  
913 megacity in Central China: Levels, sources, and variation trends, *Atmospheric Environment*, 232,  
914 117581, <https://doi.org/10.1016/j.atmosenv.2020.117581>, 2020.

915 Zhou, B., Wang, Q., Zhou, Q., Zhang, Z., Wang, G., Fang, N., Li, M., and Cao, J.: Seasonal  
916 Characteristics of Black Carbon Aerosol and its Potential Source Regions in Baoji, China, *Aerosol  
917 and Air Quality Research*, 18, 397-406, 10.4209/aaqr.2017.02.0070, 2018.

918 Zhou, Y., Ma, X., Tian, R., and Wang, K.: Seasonal transition of Black carbon aerosols over Qinghai-  
919 Tibet Plateau: Simulations with WRF-Chem, *Atmospheric Environment*, 308, 119866,  
920 <https://doi.org/10.1016/j.atmosenv.2023.119866>, 2023.

921 Zhu, C., Kanaya, Y., Takigawa, M., Ikeda, K., Tanimoto, H., Taketani, F., Miyakawa, T., Kobayashi, H.,  
922 and Pisso, I.: FLEXPART v10.1 simulation of source contributions to Arctic black carbon, *Atmos.  
923 Chem. Phys.*, 20, 1641-1656, 10.5194/acp-20-1641-2020, 2020.

924 Zhuang, B. L., Wang, T. J., Liu, J., Li, S., Xie, M., Yang, X. Q., Fu, C. B., Sun, J. N., Yin, C. Q., Liao, J. B.,  
925 Zhu, J. L., and Zhang, Y.: Continuous measurement of black carbon aerosol in urban Nanjing of  
926 Yangtze River Delta, China, *Atmospheric Environment*, 89, 415-424,  
927 <https://doi.org/10.1016/j.atmosenv.2014.02.052>, 2014.

928 Zong, Z., Wang, X., Tian, C., Chen, Y., Qu, L., Ji, L., Zhi, G., Li, J., and Zhang, G.: Source apportionment  
929 of PM<sub>2.5</sub> at a regional background site in North China using PMF linked with radiocarbon analysis:  
930 insight into the contribution of biomass burning, *Atmos. Chem. Phys.*, 16, 11249-11265,  
931 10.5194/acp-16-11249-2016, 2016.

932